Slope failure characteristics and stabilization methods

H. (Joanna) Chen and S.H. Liu

Abstract: This paper presents numerical and laboratory experiments to investigate slope failure characteristics and commonly used slope stabilization methods. Using an improved distinct element method, the interparticle adhesive force is incorporated with a modified numerical model to account for the effect of suction. The model is validated through laboratory tilting box tests. Calculated slope failure angles are consistent with experimental observations. Different patterns of slip surface are also identified. Furthermore, the modified numerical model quantifies the micromechanical characteristics of the interparticle network and their evolutions during shear deformation. The calculations show that the maximum ratio of shear stress to normal stress takes place when the contact plane coincides with the mobilized plane, whereas the minimum value occurs when it is parallel to the directions of principal stresses. On this basis, we propose the optimal installation angle of soil nails along the minor principal stress (σ_3) direction. The effectiveness of this approach is evaluated through tilting box tests. Two commonly used slope surface stabilization methods are also experimentally investigated.

Key words: distinct element method, tilting box test, slip surface, optimal installation angle of soil nails.

Résumé : Cet article présente des études numériques et des expériences en laboratoire pour étudier les caractéristiques de rupture de talus et les méthodes couramment utilisées pour la stabilisation des talus. Au moyen d'une méthode améliorée d'éléments distincts, la force d'adhésion entre les particules est incorporée dans un modèle numérique modifié pour tenir compte de l'effet de succion. Le modèle est validé par des essais d'inclinaison de boîte en laboratoire. Les angles de rupture de talus calculés sont consistants avec les observations expérimentales. Différents schémas de surface de rupture ont été identifiés. De plus, le modèle numérique modifié quantifie les caractéristiques micromécaniques du réseau interparticule et leurs évolutions durant la déformation en cisaillement. Les calculs montrent que le rapport maximum de la contrainte de cisaillement sur la contrainte normale est atteint lorsque le plan de contact coïncide avec le plan mobilisé, alors que la valeur minimale se produit lorsque ce plan est parallèle aux directions des contraintes principales. Sur cette base, nous proposons l'angle optimal d'installation des clous de sol dans la direction de la contrainte principale mineure (σ_3). L'efficacité de cette approche est évaluée au moyen des essais de boîte inclinée. On étudie aussi expérimentalement deux méthodes de stabilisation des surfaces de talus communément utilisées.

Mots-clés : méthode d'éléments distincts, essai de boîte inclinée, surface de glissement, angle optimal d'installation de clous de sol.

[Traduit par la Rédaction]

Introduction

Landslides are natural disasters that often originate in steep slopes. Expanding urbanization and changing land-use practices have increased the frequency of their occurrence. Despite improvements in recognition, prediction, and mitigative measures, natural landslides and engineered slope failures still exert a heavy social, economic, and environmental toll (e.g., McConnell and Brock 1904; Cruden and Varnes 1996; Chen and Lee 2000; Crosta et al. 2004). Fundamental aspects in the study of landslide- and slope-failure-related problems include triggering and runout mechanisms, mobility analysis, and countermeasure approaches. As slopes consist of native or transported earth materials, engineering properties and behaviours are quite variable and unpredictable to precise limits. Attention to this subject is being emphasized in theoretical study and geotechnical engineering practices.

Various slope stabilization methods exist in geotechnical engineering practices that correspond to different field conditions and economic considerations. For example, soil nailing is a method of construction that reinforces the existing ground (such as slopes and retaining walls). This is because the nails develop tension when the ground deforms laterally in response to ongoing excavation. Soil-nailing technology has been widely adopted in soil excavation and slope and retaining wall stabilization because of its cost effectiveness, rapid construction, and revision flexibility in construction process. Attention to soil–nail interaction has been largely brought to the pullout behavior of nails in sandy clay (Chai and Hayashi 2005), in loose fills with fine gravels

Received 22 March 2005. Accepted 13 November 2006. Published on the NRC Research Press Web site at cgj.nrc.ca on 3 May 2007.

H.J. Chen.[1] Golder Associates Ltd, 1000, 940–6th Avenue SW, Calgary, AB T2P 3T1, Canada.
S.H. Liu. College of Water Conservancy and Hydropower Engineering, Hohai University, Nanjing, China.

[1]Corresponding author (e-mail: Joanna_Chen@golder.com).

 doi:10.1139/T06-131

(Junaideen et al. 2004), and in loose to medium dense sand (Schlosser et al. 1992; Luo et al. 2000; Hong et al. 2003). In these cases nail installations are horizontal. The frictional resistance at the soil–nail interface is regarded as the major contribution to the soil mass stabilization (Shewbridge and Sitar 1990; Jewell and Pedley 1992; Raju et al. 1997). In some cases, the inclination angles of nails are within 10°–20° of the horizontal direction (Prior 1992; Barley 1993; Kim et al. 1995). A recent study (Güler and Bozhurt 2004) on two full-scaled nailed structures with upward and downward installations suggested that the soil-nailed structures with nails installed at angles above horizontal give better results with regards to the factor of safety. To the best knowledge of the authors, the optimal installation angle has rarely been studied in the literature.

Experimental and numerical modelling are the two important components in the study of slope failure characteristics. Experimental investigations usually deliver macroscopic information for slope failure patterns and measurable parameters. As a soil mass consists of discrete particles, microscale interaction among particles significantly influences the macromechanical behavior of soil mass. The distinct element method (DEM), which was originally designed for research into the micromechanical behavior of granular assemblies that were subject to generalized motion (Cundall 1971), has been vastly improved since its original inception and has been successfully applied to simulate the microbehaviour of interacting particles (e.g., Cundall and Strack 1979; Rothenburg and Bathurst 1989; Cundall 2000). Conventional DEM generally deals with dry granular particles exclusive of pore-water pressure. It is noted that slope failures typically occur following heavy rainfall. Rainfall infiltration perceivably results in major changes in soil suction. Conventional DEM modelling when incorporated with interparticle adhesive forces may account for the effect of soil suction. It helps us to understand slope failure mechanisms under different boundary conditions, such as rainfall-induced slope failures.

In this paper, an interparticle adhesive force is incorporated into the conventional DEM to account for the influence of capillary menisci among particles. This improved DEM is validated through laboratory tilting box tests simulating the slope failure process under plane-strain – plane-stress conditions. Calculated results quantify the micromechanical characteristics of the interparticle network and the evolution of particles during shear deformation. On this basis, we designed a series of tilting box tests to investigate some commonly applied slope-stabilization measures, with emphasis on the installation angle of the nails.

The improved distinct element model

The DEM is a numerical technique in which individual particles are represented as rigid bodies. Tracing the movement of individual particles, the interaction of assemblies of disc (two-dimensional) or spherical (three-dimensional) particles, is described as a transient problem with states of equilibrium contact forces and displacements of the stressed assemblies developing whenever the internal forces are balanced. In two dimensions, a particle has three degrees of freedom (two translational and one rotational). A particle may be in contact with the neighboring particles or structure boundaries. Particles are in contact only when the distance between the particle centers is not larger than the sum of their radii. If the displacement increments of two individual discs over a very small time interval, Δt, are represented as $(\Delta x_i, \Delta y_i, \Delta\varphi_i)$ and $(\Delta x_j, \Delta y_j, \Delta\varphi_j)$, the relative displacement increments of the two individual particles at contact may be expressed as

$$[1]\quad \begin{aligned} \Delta u_{\mathrm{N}} &= (\Delta x_i - \Delta x_j)\cos\alpha_{ij} + (\Delta y_i - \Delta y_j)\sin\alpha_{ij} \\ \Delta u_{\mathrm{S}} &= -(\Delta x_i - \Delta x_j)\sin\alpha_{ij} + (\Delta y_i - \Delta y_j) \\ &\quad \times \cos\alpha_{ij} + (r_i\Delta\varphi_i + r_j\Delta\varphi_j) \end{aligned}$$

where Δu_{N} and Δu_{S} are the normal and tangential displacements along the contact plane, respectively, Δu_{N} is positive for compression and Δu_{S} is positive for counterclockwise rotation, r_i and r_j are the radii of the two particles, and (x_i, y_i) and (x_j, y_j) are the Cartesian coordinates of the particle centroids.

The global unit vector $\boldsymbol{e} = (\cos\alpha_{ij}, \sin\alpha_{ij})$ is defined as

$$[2]\quad \begin{aligned} \sin\alpha_{ij} &= (y_j - y_i)/R_{ij} \\ \cos\alpha_{ij} &= (x_j - x_i)/R_{ij} \end{aligned}$$

normalized by the distance $R_{ij} = [(x_i - x_j)^2 + (y_i - y_j)^2]^{1/2}$.

Contact between two particles, or a particle and a boundary, is modeled by the elastic spring and viscous dashpots in both the normal and tangential directions (suffixed with N and S, respectively). The increment of the normal contact force, Δe_{N}, is caused by the relative displacement increment, Δu_{N}, and can be calculated via an elastic force – displacement law:

$$[3]\quad \Delta e_{\mathrm{N}} = k_{\mathrm{N}}\Delta u_{\mathrm{N}}$$

where k_{N} is the normal stiffness. The relative velocity $\Delta u_{\mathrm{N}}/\Delta t$ leads to the dynamic normal contact force, d_{N},

$$[4]\quad d_{\mathrm{N}} = \eta_{\mathrm{N}}\frac{\Delta u_{\mathrm{N}}}{\Delta t}$$

where η_{N} is the normal damping. The total normal contact force between two particles is given by the summation of the static and dynamic components

$$[5a]\quad [f_{\mathrm{N}}]_t = [e_{\mathrm{N}}]_t + [d_{\mathrm{N}}]_t$$

in which

$$[5b]\quad [e_{\mathrm{N}}]_t = [e_{\mathrm{N}}]_{t-\Delta t} + \Delta e_{\mathrm{N}} \quad \text{and} \quad [d_{\mathrm{N}}]_t = d_{\mathrm{N}}$$

There is no extension force at the contact surface when $[e_{\mathrm{N}}]_t < 0$ or $[e_{\mathrm{N}}]_t = [d_{\mathrm{N}}]_t = 0$.

Likewise, the total tangential contact force between two particles may be written as

$$[6a]\quad [f_{\mathrm{S}}]_t = [e_{\mathrm{S}}]_t + [d_{\mathrm{S}}]_t$$

where

$$[6b]\quad [e_{\mathrm{S}}]_t = [e_{\mathrm{S}}]_{t-\Delta t} + \Delta e_{\mathrm{S}} = [e_{\mathrm{S}}]_{t-\Delta t} + k_{\mathrm{S}}\Delta u_{\mathrm{S}}$$

$$[6c]\quad [d_{\mathrm{S}}]_t = d_{\mathrm{S}} d_{\mathrm{S}} = \eta_{\mathrm{S}}\frac{\Delta u_{\mathrm{S}}}{\Delta t}$$

In the tangential direction, the particle slides if the tangential force reaches the Coulomb friction limit. Therefore,

$$[7a] \quad [e_S]_t = [d_S]_t = 0, \quad \text{if } [e_N]_t < 0$$

$$[7b] \quad [e_S]_t = \mu [e_N]_t \times \text{sign}[e_S]_t \quad \text{and} \quad [d_S]_t = 0, \quad \text{if } \left|[e_S]_t\right| > \mu\left|[e_N]_t\right|$$

where the friction coefficient, $\mu = \tan\phi_\mu$, with ϕ_μ being the interparticle friction angle.

Once the normal and tangential forces are determined for each contact, they are projected onto the x and y directions. The summation of the force components over all contacts and the resultant moment $[M_i]_t$ are given by

$$[8a] \quad [F_{xi}]_t = \sum_j (-[f_N]_t \cos\alpha_{ij} + [f_S]_t \sin\alpha_{ij}) + m_i g_x$$

$$[8b] \quad [F_{yi}]_t = \sum_j (-[f_N]_t \sin\alpha_{ij} - [f_S]_t \cos\alpha_{ij}) + m_i g_y$$

$$[8c] \quad [M_i]_t = -r_i \sum_j ([f_S]_t)$$

where m_i and (g_x, g_y) represent the mass of a particle and the components of gravitational acceleration, respectively.

In unsaturated soils with a low degree of saturation, water partially occupies the voids of soil particles and capillary menisci build up between adjacent particles. Water attaches to the surface of some particles, as shown in Fig. 1*a*. The curved water–particle interface produces surface tension (T), which in turn generates suction (s) and interparticle adhesive force (P_S) perpendicular to the contact plane between adjacent particles (Fig. 1*b*). Assuming that the shape of the liquid bridge is a toroid characterized by radii r and b, suction across the liquid water bridge and the interparticle adhesive force are calculated in a 2D manner (Ohashi and Matsuoka 1995; Han et al. 2004) by

$$[9a] \quad s = u_a - u_w = T(1/r - 1/b)$$

$$[9b] \quad P_S = (u_a - u_w)\pi b^2 + T(2\pi b)$$

where u_a and u_w are the pore-air and pore-water pressures, respectively, and r and b are the radii of the meniscus and the capillary water cylinder at its center. The radii r and b can be expressed geometrically in term of the radius of particle R and the angle of capillary water retention, β, by $b = R(\tan\beta + 1 - \sec\beta)$ and $r = R(\sec\beta - 1)$.

We incorporate the interparticle adhesive force between two adjacent particles by

$$[10] \quad \begin{aligned} [F_{xi}^p]_t &= \sum_j P_{Sij} \cos\alpha_{ij} \\ [F_{yi}^p]_t &= \sum_j P_{Sij} \sin\alpha_{ij} \\ [M_i^p]_t &= 0 \end{aligned}$$

and add it to eq. [8] for the total net forces. Newton's second law was applied to trace the motion of a particle resulting from the contact forces and momentum, and the accelerations are given by

$$[11] \quad [\ddot{\mathbf{X}}_i]_t = \frac{[\mathbf{F}_{Xi}]_t + [\mathbf{F}_{Xi}^p]_t}{m_i}; \qquad [\ddot{\varphi}_i]_t = \frac{[M_i]_t}{I_i}$$

where $\mathbf{X}_i = (x_i, y_i)$, $\mathbf{F} = (F_x, F_y)$, and I_i and φ_i represent the moment of inertia and angular displacement of a particle, respectively. The velocity and displacement can be integrated using an explicit central difference scheme.

The mean stress is calculated from the interparticle contact forces by (Christoffersen et al. 1981)

$$[12] \quad \sigma_{ij} = \left(\sum_\Omega l_i F_j\right) \Big/ V$$

where Ω is the calculation domain, V is the volume of the domain, l_i is the length of the vectors connecting the centers of contacting particles, and F_j is the contact force. The above procedure has been formulated in a computer program, GRADIA (Yamamoto 1995), which was validated through the comparisons with the experimental tests conducted in the next section.

Tilting Box Test (TBT)

The slope-failure characteristics were investigated through the observation of the movement of an assembly of aluminum rods contained in a titling box. As sketched in Fig. 2, the titling box was rectangular: 82 cm in length and 30 cm in both height and width. The front and back walls of the tilting box were removable to allow for an adjustable width. The front wall was transparent (glass) for the convenience of observation. Driven upwards by an electric motor, the box could be adjusted gradually to a maximum inclination of 60°. An assembly of aluminum rods was used to construct a slope inside the tilting box. The rod assembly can stand up under its own weight without any external support and subsequently no frictional resistance would be produced on the front or back wall of the tilting box. The movement of the aluminum rods could be traced visually by placing a mark on the front surface of the constructed slope.

Two assemblies of cylindrical aluminum rods (50 mm long) were used. The first assembly comprised a mixture with diameters of 5.0 and 9.0 mm (henceforth, type I). The second assembly had diameters of 1.6 and 3.0 mm (henceforth, type II). The weight ratio of type I rods refers to the ratio of the weight of the 9.0 mm rods to that of the 5.0 mm rods. The weight ratio of type II rods is defined as ratio of the weight of the 3.0 mm rods to that of the 1.6 mm rods. The proportions of the larger and smaller rods for type I and type II were the same as their weight ratio, 3:2. These two types of mixed assemblies had the same specific gravity of 2.69, a void ratio of 0.201, and a dry density of 21.6 kN/m^3. The diameters of type I and type II rods were in the size range of fine gravel and medium to coarse sand, respectively. The specific gravity was close to that of quartz chips (about 2.65).

Testing in a dry state

The type I assembly was arranged to construct a slope inside the tilting box whose front and back walls were removed after the setup. Colour lines were drawn on the front surface of the rods so that their movement could be easily observed and traced as the box was gradually tilted at a constant angular speed of 1°/min. The failure process of the dry aluminum-rod slope is shown in Fig. 3. It was observed that the particle movement began along the slope surface, gradu-

Fig. 1. (*a*) Water attached to aluminum rods, capillary menisci buildup (after Ohashi and Matsuoka 1995). (*b*) Sketch of the interparticle adhesive force due to the surface tension of capillary water.

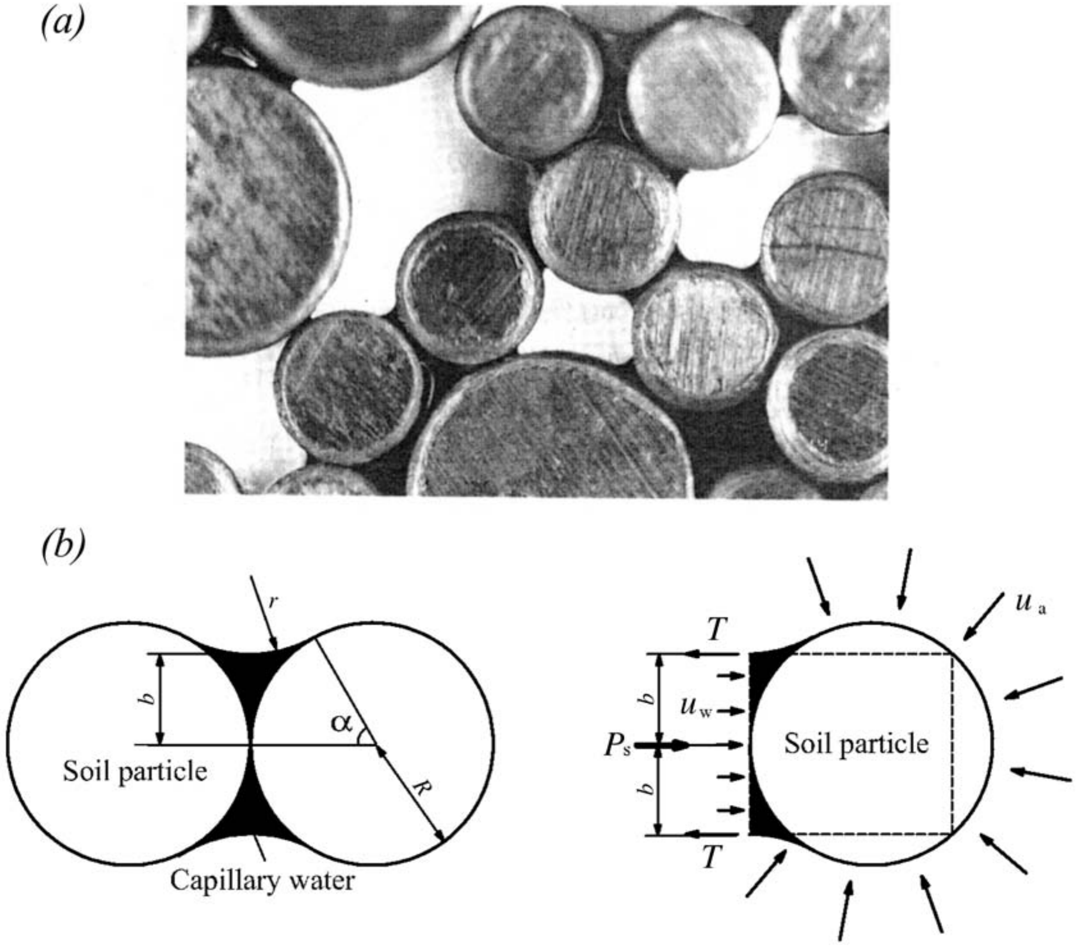

Fig. 2. Setup for the titling box tests.

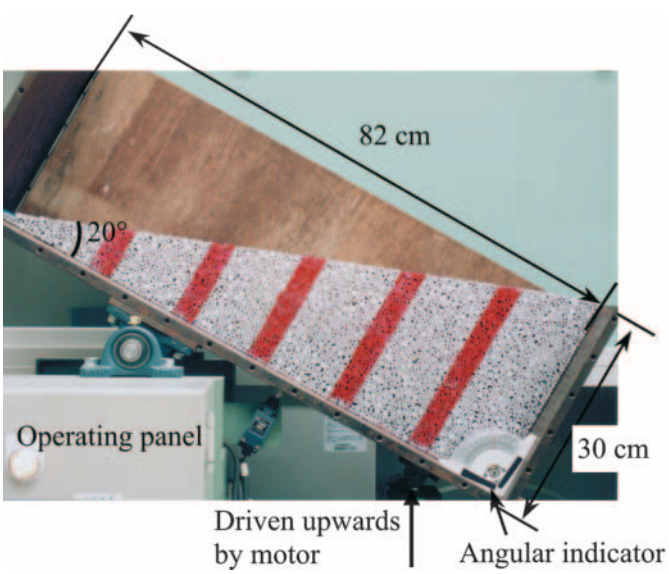

ally developing to a certain depth, and eventually shaped as a shallow slip plane beneath the slope surface. The failure angle was defined to be the inclination of the slope when visible initial movement of the rods occurred. It was recorded as 24.5° in this case. The mean failure depth was around 3.0 cm (case A1). The above test procedures were repeated on the type II rods in a dry state (case B1). The failure angles ranged between 24.0° and 26.6°. The failure pattern was similar to case A1. Comparisons were made with some previous laboratory tests by Matsuoka et al. (1999) using materials such as Toyoura sand (0.10–0.30 mm, e_0 = 0.71), glass beads (0.355–0.60 mm, e_0 = 0.62), and crushed sand (0.42–2.0 mm, e_0 = 0.82) in dry states. A similar failure pattern was shown in these tests where the failed body always formed a shallow slip plane rather than a circular arc.

Testing in a moist state

Type I and type II assemblies were submerged with water in a bucket. The wetted rods were taken out of water and constructed to a slope inside the tilting box. A film of water was readily visible around some rod surfaces, but no free water was present. Similar test procedures were carried out in the TBT of A2 and B2, in which the water content (w) was equal to 1.4%. The rods were observed to move when the box was inclined up to 29.5° (about 5° higher than the relevant one in the dry state). As shown in Fig. 4 (type II), the slip surface exhibited a circular arc as commonly observed in cohesive soil slopes. The maximum failure depth was around 10 cm. The failure angles of test

Fig. 3. Sequence of the failure process of the dry aluminum rod slope (type I): (*a*) → (*b*) → (*c*).

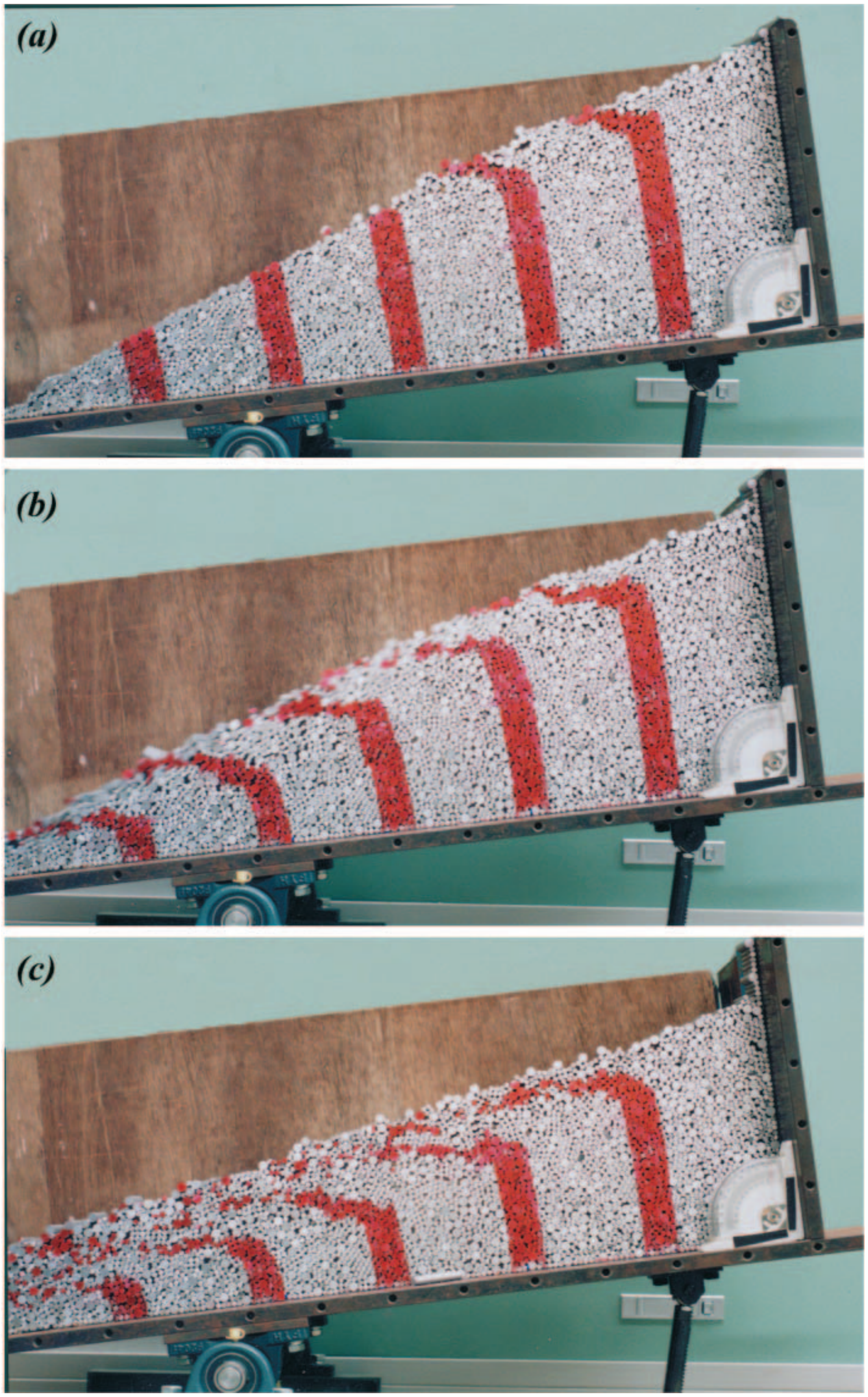

cases A1, A2, B1, and B2 using aluminum rods are summarized in Table 1. The above testing procedures were applied to Toyoura sand (w = 2.9%), which was wetted in the similar way. The front and back walls of the tilting box were adjusted to the maximum width of 30 cm and their inner sides were lubricated so as to minimize the friction between the walls and the testing materials. The failure angles ranged from 48.2° to 48.7°, considerably higher than the dry state angles of 33°–36°. The failure slip surface showed a circular arc. We recognized that the slip plane with shallow depth occurred in dry conditions without cohesion, while the circular slip surface with shallow depth took place in moist conditions.

Numerical validations

The proposed numerical model was validated through the simulation of the above TBT on type I aluminum rods. As

Fig. 4. Failure pattern of the moist aluminum rod slope (type II).

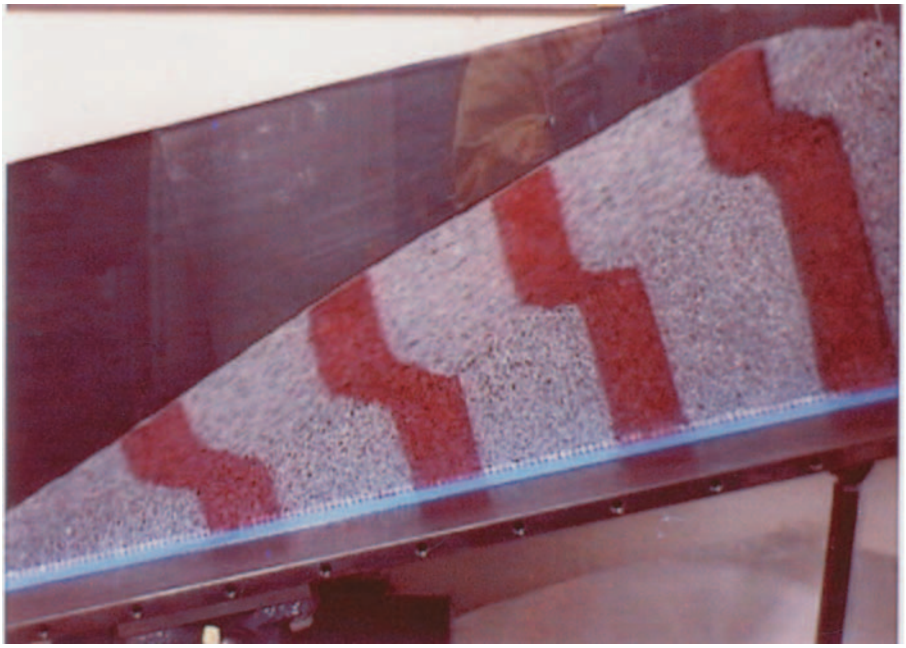

Table 1. Tilting box tests using aluminum rod assemblies.

Case	Material	State	Slope length (cm)	Slope angle at failure (°)
A1	Type I assembly: 9 and 5 mm aluminum rods mixed in a 3:2 proportion	Dry, moist (w = 1.4%)	80–86	23.0–25.0
A2	Type I assembly: 9 and 5 mm aluminum rods mixed in a 3:2 proportion	Dry, moist (w = 1.4%)	80–86	29.0–29.5
B1	Type II assembly: 3 and 1.6 mm aluminum rods mixed in a 3:2 proportion	Dry, moist (w = 1.4%)	80–86	24.0–26.5
B2	Type II assembly: 3 and 1.6 mm aluminum rods mixed in a 3:2 proportion	Dry, moist (w = 1.4%)	80–86	29.0–29.5

shown in Fig. 5, the initial particle distributions for the simulations were created and digitized based on the exact arrangements of the rods in the above tests in terms of rod size, distribution, and total number.

Slope failures in a dry state

The input parameters of the DEM simulations of type I rods in a dry state are listed in Table 2, corresponding to the properties of the rod assembly used in the experiments. The interparticle adhesive force, P_S, was equal to 0. The stiffness and the damping parameters are based on the contact theory of two elastic discs by considering the stress level possibly applied on rod particles; the interparticle friction angle, ϕ_μ = 16°, was obtained from the frictional tests on the aluminum rods. These parameters have been used to simulate biaxial compression test, simple- and direct-shear tests on an assembly of aluminum rods (Yamamoto 1995; Liu and Matsuoka 2003; Liu et al. 2003). The computed failure angle was 25°, within the ranges measured from the conducted TBT (case A1). To exclude the boundary effect, the midportion along the slope surface with a length of 60 cm was analyzed. For clarity, the mid-slope had a grid at every 10 cm parallel to the slope surface with 9 mm in depth (see Fig. 6). The mean displacement of the particles within a mesh represents the gross movement in this region. During shear deformation, the cohesionless assemblies exhibited a continuous change in the evolution of interparticle forces. Figure 6*a* shows the calculated particle displacements at failure with the interparticle contact information along the mobilized plane. It is seen that the particles move almost parallel to the slope surface, similar to the simple-shear deformation with a shallow depth. Corresponding to the relevant depth of the region, the statistical distribution of the mean mobilized friction angles is shown in Fig. 6*b*, calculated by

$$[13] \qquad \tan\phi_{\mathrm{mo}} = \frac{\sum_{i=1}^{n} f_i \sin(\theta_i + \phi_{\mu\mathrm{mo},i})}{\sum_{i=1}^{n} f_i \cos(\theta_i + \phi_{\mu\mathrm{mo},i})}$$

in which θ is the interparticle contact angle defined as the angle between the contact plane and the plane parallel to the slope surface, f is the interparticle contact force, $\phi_{\mu\mathrm{mo}}$ is the

Fig. 5. Initial particle distribution in the distinct element method (DEM) simulation, reproducing the initial distribution of the type I assembly in Fig. 1.

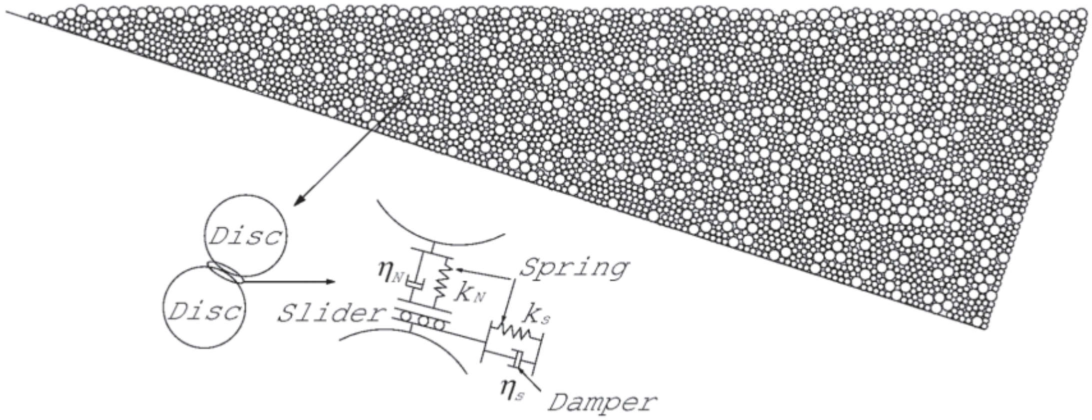

Table 2. Input parameters for the distinct element method (DEM) simulations.

Parameter	Value
Normal stiffness, k_N (N/m^2)	9.0×10^9
Shear stiffness, k_S (N/m^2)	3.0×10^8
Normal damping, η_N (N s m^{-2})	7.9×10^4
Shear damping, η_S (N s m^{-2})	1.4×10^4
Interparticle friction angle, ϕ_μ (°)	16
Density of particles, ρ (kg/m^3)	2700
Time increment, Δt (s)	2×10^{-7}
Interparticle adhesive force, P_S (N)	0–0.2

interparticle mobilized friction angle, and i is the particle contact number. The calculated mean mobilized friction angle within the deformed area was between 22° and 25°.

The orientation of principal stresses was calculated by eq. [12] and is shown in Fig. 6*c*. At peak state, the major principal stress was roughly inclined to the slope surface at an angle of 32.5°. The internal friction angle of granular material follows the common definition, $\phi = \tan^{-1}(\tau/\sigma_N)$, where τ is the shear stress and σ_N is the normal stress. The internal friction angle of the aluminum rod system herein was obtained from direct shear tests, ranging between 22° and 24°. The angle between the mobilized plane and the major principal stress was equal to $(\pi/4 - \phi/2)$, ranging from 33° to 34° in the present case. This value approaches the angle between the major principal stress and the slope surface. Subsequently, the mobilized plane parallels with the slope surface, and the particles within the midportion of the slope move along the slope surface. The calculation agrees with the experimental observations that the slip plane parallels the slope surface. The number of the particle contact with respect to an angle, α, can be recorded during the shearing, where α is the inclination between the particle contact normal direction and the mobilized plane. As illustrated in Fig. 6*c*, the frequency distribution of the contact orientation, $M(\alpha)$, tends to a preferred direction that gradually rotates with the increase of shear stress more rapidly than other directions. This preferred direction coincides with the major principal stress axis. It agrees with similar observations in simple-shear tests on photoelastic rods by Oda and Konishi (1974*a*, 1974*b*).

Shearing deformation also leads to the change of the numbers of interparticle contacts. With respect to the possible range of contact angle θ, the number of interparticle contacts $N(\theta)$ was monitored during the slope-tilting process. Figure 7 shows the normalized frequency distribution of the number of interparticle contacts, $N(\theta)/N_{max}$, parallel to the slope surface in accordance with Fig. 6. It was noted that the distribution shifts to the right side as the slope angle increases, suggesting that the number of particle contacts increases in the positive zone of θ. We further define the frequency distribution for the newly generated contact normal stresses as $N_g(\theta)$ and for those have just disappeared as $N_d(\theta)$. As was evident in Fig. 8, $N_d(\theta)$ is concentrated in the negative zone of θ and $N_g(\theta)$ is more frequent for positive θ. This suggests that the number of interparticle contacts increases with the tilting of the slope angle, and the interparticle contact angle is effective to the resistance of shearing.

The change of the interparticle contact angle along the mobilized plane (parallel to the slope surface) is traced in Fig. 9 during the tilting of the slope until failure. The solid curve represents the ratio of shear stress to normal stress on the contact plane. The contact angle along the mobilized plane is observed proportional to this ratio, suggesting that the frictional law on the contact plane controls the movements of particles on the mobilized plane. The maximum value of this ratio takes place when the contact plane coincides with the mobilized plane (θ = 0), and the minimum value occurs when it is parallel to the directions of principal stresses. This scenario agrees with the information conveyed in Fig. 6. This information is meaningful to the design of slope-stabilization measures including the optimal installation angle of soil–nails and will be discussed in the Experimental study section.

It is noteworthy that the change of interparticle friction may have a limited influence on the internal friction angle; the global internal friction angle increases with the interparticle angle at a very small value, but is essentially constant for a larger value of interparticle angle (e.g., Skinner 1969; Cambou et al. 1993; Oger et al. 1998).

Fig. 6. Numerical simulations of the dry aluminum rod slope at failure (failure angle = 25°): (*a*) particle displacement; (*b*) mean mobilized friction angles corresponding to the relevant depth; and (*c*) frequency distribution, $M(\alpha)$, of particle contacts along the contact normal direction and orientation tendency of principal stresses.

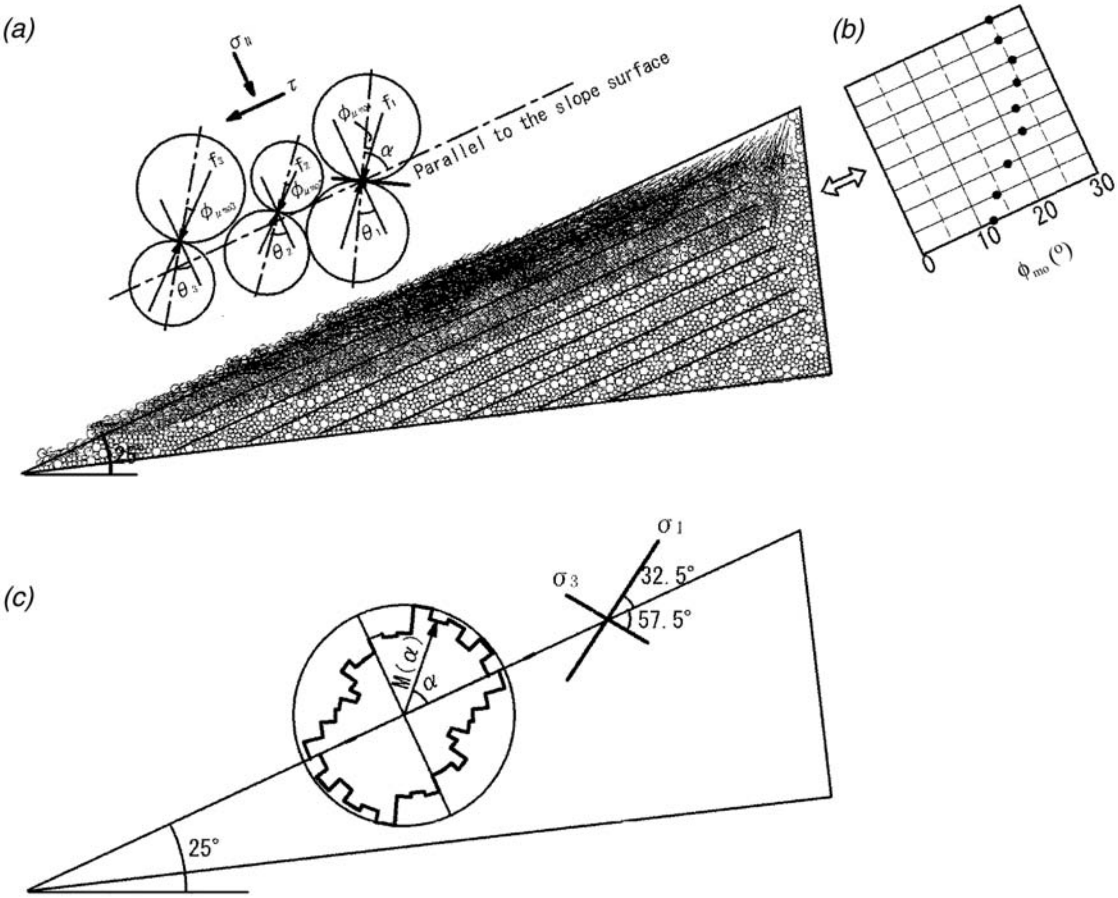

Fig. 7. Variation of contact angles on planes parallel to the slope surface during the tilting of the box until failure; solid line, before titling; dashed line, tilting to the slope angle of 25°.

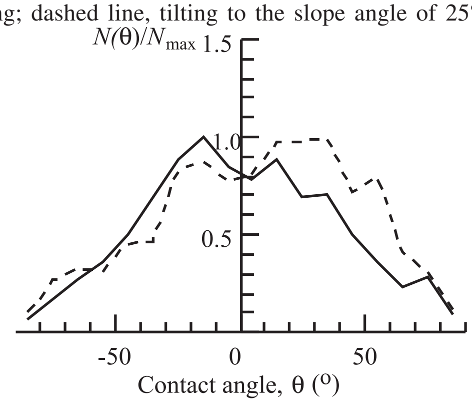

Slope failures in a moist state

The adhesive force between particles is introduced by the surface tension of water where capillary menisci build up between adjacent particles. The adhesive force at each contact point among particles may vary depending on the size, shape, and pore-water state inside the voids of soils. To simulate the performed TBT on type I in moist conditions (case A1), P_S was made constant for simplicity in the present calculation. The moisture content of the wetted rods was 1.4%, which is equivalent to a degree of saturation of 0.185, provided that the specific gravity is 2.65 and that the void ratio is 0.201. Referenced to Han et al. (2004), the possible maximum value of the capillary force of sand is around 0.5 N, and the capillary force rapidly decreases to zero when the degree of saturation increases to 0.34. In the current case, P_S is taken as 0.2 N and other input parameters are the same as those listed in Table 2. The calculated slope failure angle of 30° matches with the value from the TBT of case A1. The failure-depth distribution and the particle movements are shown in Fig. 10, where the slip surface is circular as observed in the TBT (case A2).

Furthermore, the values of P_S decrease from 0.2 to 0 N with an interval of 0.05 N. The slope angle was set as 25°. For a given P_S, typical patterns of particle movements are presented in Fig. 11. The displacements of particles along the slope surface increase with decreasing P_S. For $P_S = 0$, equivalent to the dry state without cohesion, the slope failed. The slope-failure angles are consistent with the experimental measurements. Corresponding to different values of P_S in multiple runs, the ratio $F_S = \tan\phi/\tan\phi_{mo}$ were computed, where ϕ_{mo} is the distribution of the mean mobilized friction angles related to the failure depth according to eq. [13], and

Fig. 8. Particle contact information for disappearance and generation on the planes parallel to the slope surface.

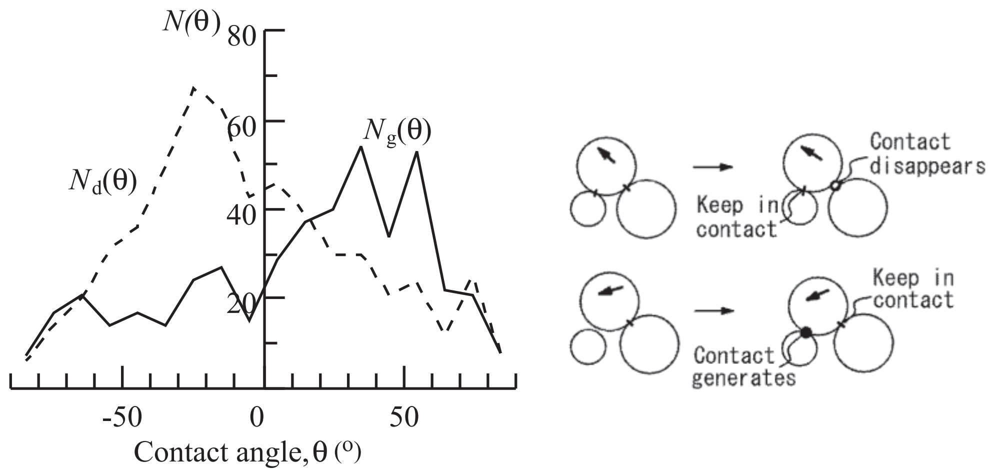

Fig. 9. Variation of the interparticle contact angle along the mobilized plane during the tilting of the slope until failure (circular plots) and their fitting with the ratio of the shear stress to the normal stress on the contact plane (solid curve).

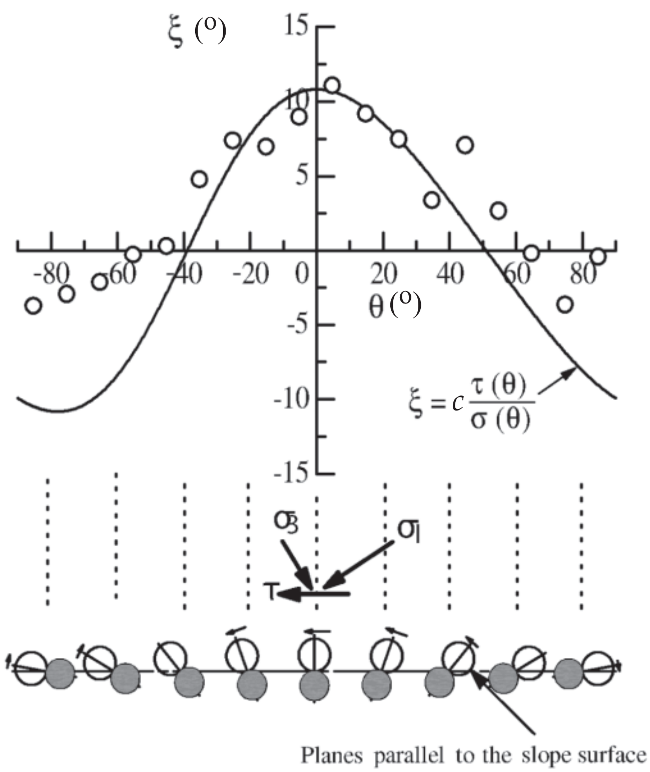

ϕ is the internal friction angle of the slope materials (aluminum rods, $\phi = 22°–24°$ obtained from direct-shear tests). It is apparent that P_S plays an important role in F_S, which in a certain sense may be considered as a safety measure for slopes.

When rainfall infiltrates dry soils, rainwater leads to a temporary change in soil suction in slopes above groundwater level. Within the infiltrated area, only a certain amount of water enters the soils during a storm and only a limited zone of soil is wetted. In thick mantle soils, the shear stress of the upper zone is reduced, but the deeper soil is relatively unaffected. Slope failures in this situation commonly occur within a certain depth. This is especially true in some regions where many rainfall-induced slope failures are usually minor in volume and shallow in depth (Chen and Lee 2004), although in slope stability analysis, the failed body has been commonly assumed as a complete rigid body failure with circular slip surface. As illustrated in Fig. 12*a*, a shallow failure occurred in the slope and the trees inclined towards the major descendent direction of the slope rather than its crest. Only if the failed body is assumed rigid and the failure plane is assumed circular may the tree incline towards the slope crest (see Fig. 12*b*).

Soil suction can be found in a slope that lies above the water table. The meniscus formed between adjacent soil particles by the soil suction creates a normal force between the particles, which bonds them in a temporary way. By the time the residual water content of soil is reached, the increase in matric suction contributes a significant component to the shear strength. Thus, the soil suction, if it can be relied upon, may enhance the slope stability. Nevertheless, soil suction also provides an attractive force for free water. When a slope failure is shallow and results simply from a gradual decrease of suction, the soil dilates as a low net stress is applied. In the shearing zone, dilation causes the reduction of pore-water pressure, which increases the effective stress and in turn strengthens the soil mass. On the other hand, dilation also leads to a higher void ratio. The effective stress increases until the negative excess pore-water pressure is dissipated by water flowing into the expanding void, and this serves to lower the soil strength. If the lowering of the soil strength has a magnitude larger than the increment caused by dilation, the soil becomes brittle (Chen et al. 2004). A stable slope under normal conditions may become unstable because of boundary condition changes, such as a sufficient increase of pore-water pressure. The volumetric deformation that the soil suffered is caused by the soil structure rearrangement and the occurrence of local shearing of grains in response to the suction reduction, which is in turn affected by the change of suction and the applied external force. The relationship of interparticle adhesive force with suction is beyond our current study.

Fig. 10. Failure depth distribution and the particle movements of the moist aluminum rod slope (type II, P_S = 0.2 N).

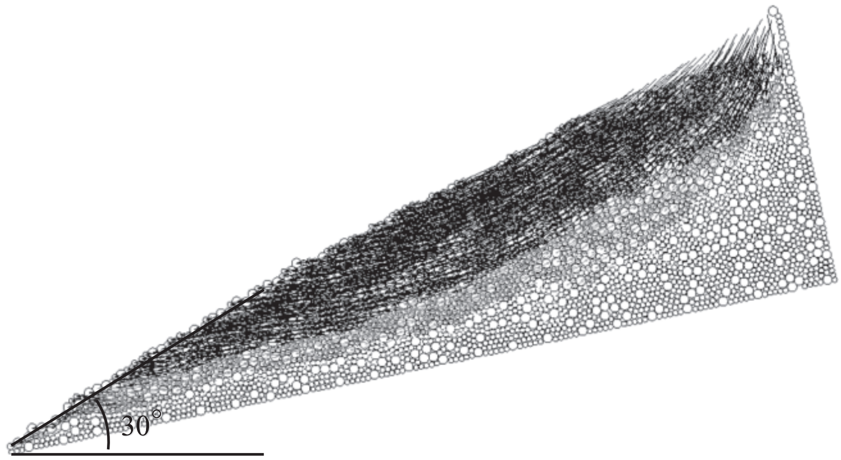

Fig. 11. Interparticle cohesive force, P_S, decreasing from 0.2 to 0.0 N.

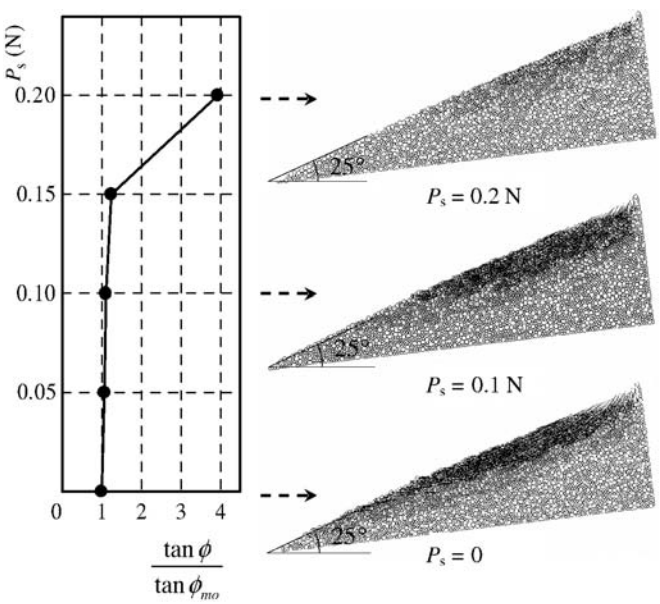

Experimental study of slope-stabilization methods

Optimal installation angle of soil nails

The DEM calculations in the previous seciton reveal that the frictional law on the contact plane governs the movement of particles on the mobilized plane. The minimum ratio of the shear stress to normal stress takes place when the contact plane is parallel to the principal stresses. For the aluminum rod assemblies in the present study, the major principal stress at peak state is inclined to the slope surface at 32.5° (see Fig. 6). Bearing this in mind, we designed two series of TBT for testing the optimal installation angle of nails.

In the first series of tests, the type II rod assembly was used to construct a slope inside the tilting box. Five pieces of thin aluminum sheet were inserted perpendicular to the slope surface (case D1), acting as nails in the 2D manner. Each aluminum sheet was 10 cm long and 5 cm wide. The inserted depth was 10 cm. The surface of the aluminum sheet was rough so as to achieve a higher shear resistance. Under similar tilting procedures, the measured failure angle was between 27° and 29° (Fig. 13). Another series of TBT was conducted with the same aluminum sheets, but installed along the σ_3 direction (case D2, same insert depth). As shown in Fig. 14, the angle between the aluminum sheets and the slope surface was 57.5° (= 90° – 32.5°). The failure angle was now between 29° and 32°, higher than that of case D1. The above experimental results are summarized in Table 3.

The shear resistance predominantly consists of two components: the one arising from the frictional sliding between particles and another from interlocking between particles and nails (Luo et al. 2000). In the above experimental settings, when shear failure takes place between particles, a considerable degree of interlocking between particles has to be overcome owing to the rough surface of the nails. With the increase of tilting, the particles being sheared around the nails tend to slide and roll, resulting in dilation in the vicinity of a nail because of the loose state of the particles and the low magnitude of confining pressure. The surrounding particles restrict such a tendency, leading to an increase of normal stress on the surrounding surface of the nail. The shear resistance on the interface between the nail and the particles is essentially governed by the dilation behavior of the particles (Xanthako 1991). On the other hand, the apparent friction coefficient diminishes with increasing normal stress. When the tilting angle continues to increase, the particles around the nails will collapse (move) beyond the maximum frictional resistance. The particle volume then contracts rather than dilates, and the dilation effect on the apparent friction might completely vanish (Luo et al. 2000). If the nails are installed along the σ_3 direction with the minimum shear to normal stress ratio, the interparticle contact plane is parallel to the principal stresses. As the frictional law on the contact plane controls the movements of the particles on the mobilized plane, the maximum frictional resistance could be achieved. Moreover, the reinforced materials should be placed in the most extensible direction where the reinforced materials might develop maximum tensile defor-

Fig. 12. (*a*) Shallow failure along the descendent slope direction and (*b*) when the failed body was assumed as rigid and the failure plane was assumed as circular, the tree inclined towards the slope crest.

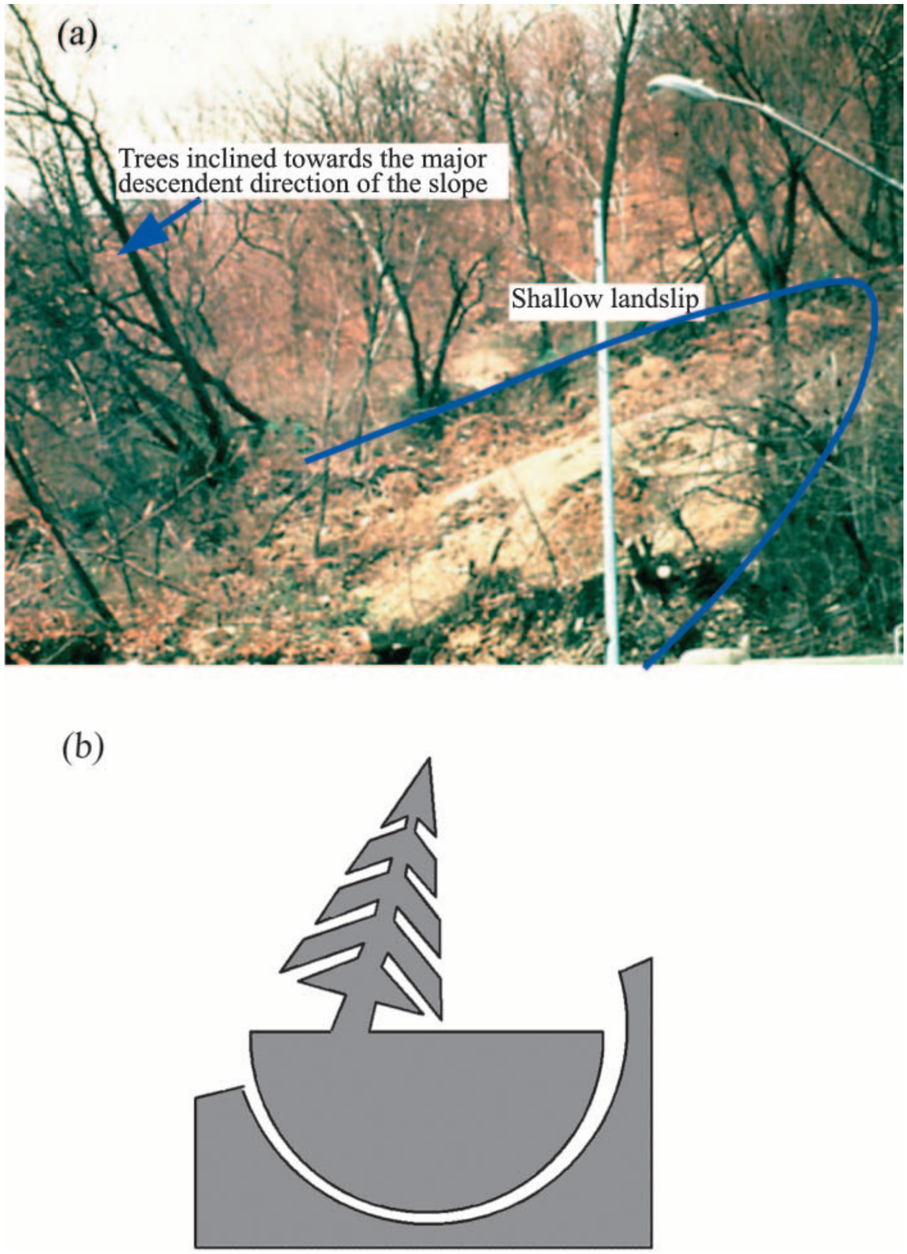

mation. Therefore, it is expected that placing the nails along the direction of the minor principal strain would be the most effective way to stabilize slopes.

These primary laboratory tests aimed to qualitatively analyze the installation angle of the nails. The aluminum sheets were inserted into the slope model without any grouting. In practical installation, soil nails are generally steel bars that can resist tensile and shear stresses and bending moment. Once the nails are in place, the structures are sprayed with shotcrete and covered with precast textured panels. Cement grouting is injected during the installation of some types of nails (such as grouted nails and jet-grouted nails). These methods would further increase the pullout resistance of the composite, and the nails are corrosion-resistant. Due to the variety of field materials and the complexity of the interaction mechanism between the apparent friction and dilatancy, further research work is being conducted on this subject.

Slope-surface stabilization

The experimental and numerical simulations in the previous section also show that the failure pattern in a dry slope is basically a slip plane roughly parallel to the slope surface. In a moist state without free water, the failure slip surface shows a circular arc. In both cases, the failure depths are shallow. We, therefore, considered stabilizing the mantle soils along the slope surface so as to minimize the movement of the soil particles.

The TBT were carried out using the type II aluminum rods to construct a slope inside the titling box. Ten strips of gum tape (15 cm × 2.5 cm) were, respectively, pasted on the

Fig. 13. Photo at failure: five pieces of thin aluminum sheets, simulating soil nails, were inserted perpendicular to slope surface (insert depth, 10 cm).

Fig. 14. Photo at failure: five pieces of thin aluminum sheets, simulating soil nails, were inserted along the σ_3 direction (insert depth, 10 cm).

front and the back faces of the slope along the descendent direction of the slope without any restraint at the toe (case C1). The length of the slope surface with gum tape was 75 cm (about 85% of the full slope-surface length of 86 cm), including the minor interval between two strips of gum tapes. The slope failure was triggered by tilting the box at an angular speed of 1°/min. Failure began locally around the slope toe and extended backwards to the mid-slope portion (Fig. 15). In a dry state, the mean slope failure angle was about 27°–29°, slightly higher than that without the sticky gum-taped stabilization (24°–26.5°) described in the DEM section (case B1). The failure depth was shallow, in the range of 2–3 cm. Failure occurred along a slip plane rather than in a circular arc. In the sense of force analysis, one could imagine the sliding body as a sandwich, confined by the upper reinforced material and the slope beneath the slip surface. Frictional resistance exists for any relative movement along the upper and lower interfaces of the sliding body, which increases slope stability, although the effect of the frictional resistance may not be very significant.

As for the failure initiated in the toe area, we conducted another series of TBTs to evaluate the influence of the downslope retaining wall together with the slope-surface stabilizing measures. Ten strips of gum tape were pasted, respectively, on the front and back faces of the slope along the descendent direction, as in case C1, except that a thick block was installed at the slope toe where a small portion of the slope was cut (case C2). There was no obvious gap between the slope and the downslope block. The failure began with the sliding of the reinforced cover, followed by the movement beneath the cover. It is surprising that the slope-failure angle increased up to 31°–32° (Fig. 16). This is substantially larger than the previous tests with only the gum-taped stabilizing surface (case C1, 27°–29°) or without any surface-stabilizing measures (case B1, 24°–26.5°).

Using rock, coarse stone, or boulders as rigid cover on soil slope surfaces, riprap is one of the commonly used stabilization methods in engineering practice. Its effectiveness can be enhanced with native plant species and re-established vegetations. A filter layer under the riprap is necessary to relieve the hydrostatic pressure inside the slope, to distribute the weight of the riprap, to prevent settling, and to prevent fine materials in the slope from being removed by hydraulic action. The filter material can be fabric, gravel, crushed stone, or small rock. Besides, riprap provides slope surface erosion control that will improve the slope stability. In some regions, the practice of upgrading loose fill slopes is to re-compact the top layer of mantle soil to 95% of the maximum

Table 3. Tilting box tests using type II aluminum rods in a dry state.

Case	Stabilization methods		Slope angle at failure (°)
B1		No stabilization measures	24−26.5
C1		Ten strips of gum tape pasted on both the front and the back faces of the slope along the descendent direction, no restraint at slope toe	27−29
C2		Similar to Case C1, except one rectangle block is placed at the slope toe acting as a retaining wall	31−32
D1	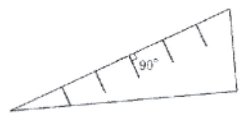	Five pieces of thin aluminum sheets inserted perpendicular to the slope surface	27−29
D2	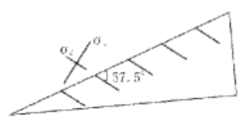	Five pieces of thin aluminum sheets inserted along the minor principal stress, σ_3, direction	29−32

Fig. 15. Photo at failure: 10 strips of gum tape (15 cm × 2.5 cm) were pasted on the front and back faces of the slope along the descendent slope direction; no restraint at the slope toe.

dry density (Chen et al. 2004). Recompaction has been proven effective in stabilizing fill slopes; static liquefaction of the fill would be very unlikely, although it could not be completely ruled out. It is noted that the experiments also show that most of the failures begin at the slope toes. Retaining walls constructed at the toe of a slope may mitigate and (or) prevent small size or secondary landslips that often occur along the toe portions. For large-scale earth movement, however, crib walls might be more effective than the conventional reinforced concrete retaining walls.

Concluding remarks

The incorporation of interparticle adhesive force was coded into the conventional DEM to account for the effect of suction. This improved DEM was validated through laboratory tilting box tests in which slope failure was simulated using aluminum rod assemblies. The simulations agree with the laboratory test results that the failure pattern of a dry slope largely shows a slip plane parallel to the slope surface, but a circular slip surface in a moist slope. Both failures are shallow in depth. Furthermore, the numerical simulations reveal microscopic information such as particle movement, including the interparticle force and contact angle, the mobilized friction angle, the principal and contact normal stresses, and the development of contact angle along the mobilized plane. The interparticle network shows that the maximum ratio of shear stress to normal stress takes place when the interparticle contact plane coincides with the mobilized plane, and the minimum value of this ratio occurs when the contact plane is parallel to the directions of principal stresses. This paper shows that the micromechanical charac-

Fig. 16. Photo at failure: 10 strips of gum tape (15 cm × 2.5 cm) were pasted on the front and back faces of the slope along the descendent slope direction. A thick block was installed at the slope toe acting as a retaining wall.

teristics of granular materials in shear deformation are pertinent to the design of slope stability measures. On this basis, the effectiveness of slope surface and soil–nail stabilization methods has been experimentally evaluated. Specifically, we showed that the optimal installation angle of soil nails is along the minor principal stress direction so that the reinforced material might develop maximum tensile deformation.

Acknowledgements

The authors are grateful to Professor H. Matsuoka of the Nagoya Institute of Technology, Nagoya, Japan, for his persistent guidance and inspiration to the study reported herein. The following financial supports are deeply appreciated by the authors: the Japan Society for the Promotion of Science (JSPS) for H. Chen, and the National Natural Science Foundation of China (grant 10672050) and Hohai University, P.R. China (grant 2084/4040110) for S.H. Liu.

References

Barley, A.D. 1993. Soil nailing case histories and developments. Retaining structures. *Edited by* C.R.I. Clayton. ICE, Thomas Telford, London.

Cambou, B., Sidoroff, F., Mahbouhir, A., and Dubujet, Ph. 1993. Distribution of micro variables in granular media, consequences on the global behavior. *In* Modern approaches to plasticity. *Edited by* D. Kolymbas. Elservier Science Publisher, Amsterdam. pp. 199–212.

Chai, X.J., and Hayashi, S. 2005. Effect of constrained dilatancy on pull-out resistance of nails in sandy clay. Ground Improvement, **9**(3): 127–135.

Chen, H., and Lee, C.F. 2000. Numerical simulation of debris flows. Canadian Geotechnical Journal, **37**: 146–160.

Chen, H., and Lee, C.F. 2004. Geohazards of slope mass movement and its prevention in Hong Kong. Journal of Engineering Geology, **76**: 3–25.

Chen, H., Lee, C.F., and Law, K.T. 2004. Causative mechanisms of rainfall-induced fill-slope failures. Journal of Geotechnical and Geoenvironmental Engineering, ASCE, **130**: 593–602.

Christoffersen, J., Mehrabadi, M.M., and Nemat-Nasser, S. 1981. A micromechanical description of granular material behavior. Journal of Applied Mechanics, ASME, **48**(2): 339–344.

Crosta, G.B., Chen, H., and Lee, C.F. 2004. Replay of the 1987 Val Pola Landslide, Italian Alps. Geomorphology, **60**: 127–146.

Cruden, D.M., and Varnes, D.J. 1996. Landslide types and processes. *In* Landslide investigation and mitigation. Vol. 3. *Edited by* A.K. Turner and R.L. Schuster. Transportation Research Board, US National Research Council, Washington, D.C. Special Report 247. pp. 36–75.

Cundall, P.A. 1971. A computer model for simulating progressive, large-scale movements in blocky rock systems. *In* Proceedings of the International Symposium on Rock Mechanics, ISRM, Nancy, France. Vol. 2, pp. 129–136.

Cundall, P.A. 2000. A discontinuous future for numerical modelling in geomechanics? Journal of Geotechnical Engineering, **149**(1): 41–47.

Cundall, P.A., and Strack, O.D.L. 1979. A discrete numerical model for granular assemblies. Géotechnique, **29**(1): 47–65.

Güler, E., and Bozhurt, C.F. 2004. The effect of upward nail inclination to the stability of soil nailed structures. *In* Geotechnical Engineering for Transportation Projects: Proceedings of Geotrans 2004 Conference, Los Angeles, California, 27–31 July 2004. American Society of Civil Engineers, Reston, Virginia. pp. 2213–2220.

Han, G., Dusseault, M.B., and Cook, J. 2004. Why sand fails after water breakthrough. Gulf Rock 2004 — Rock mechanics across borders and disciplines. *In* Proceedings of the 6th North American Rock Mechanics Symposium, NARMS 04-505, Houston, Texas, 5–10 June 2004. *Edited by* D.P. Yale, S.M. Willson, and A.S. Abou-Sayed. American Rock Mechanics Association, Alexandria, Virginia. pp. 1–9.

Hong, Y.S., Wu, C.S., and Yang, S.H. 2003. Pullout resistance of single and double nails in a model sandbox. Canadian Geotechnical Journal, **40**: 1039–1047.

Jewell, R.A., and Pedley, M.J. 1992. Analysis for soil reinforcement with bending stiffness. Journal of Geotechnical Engineering, ASCE, **118**(10): 1505–1528.

Junaideen, S.M., Tham, L.G., Law, K.T., Lee, C.F., and Yue, Z.Q. 2004. Laboratory study of soil–nail interaction in loose, completely decomposed granite. Canadian Geotechnical Journal, **41**: 274–286.

Kim, D.S., Juran, I., Nasimov, R., and Drabkin, S. 1995. Model study on the failure mechanism of soil-nailed structure under surcharge loading. Geotechnical Testing Journal, ASTM, **18**(4): 421–430.

Liu, S.H., and Matsuoka, H. 2003. Microscopic interpretation on a stress–dilatancy relationship of granular materials. Soils and Foundations, **43**(3): 73–84.

Liu, S.H., Sun, D.A., and Wang, Y.S. 2003. Numerical study of soil collapse behavior by discrete element modelling. Computers and Geotechnics, **30**: 399–408.

Luo, S.Q., Tan, S.A., and Yong, K.Y. 2000. Pull-out resistance mechanism of a soil nail reinforcement in dilative soils. Soils and Foundations, **40**(1): 47–56.

Matsuoka, H., Liu, S.H., and Ohashi, T. 1999. Model test on granular soil slope and determination of strength parameters under low confining stress near slope surface. In Proceedings of the International Symposium on Slope Stability Engineering: Geotechnical and Geoenvironmental Aspects, IS-Shikoku'99, Matsuyama, Shikoku, Japan, 8–11 November 1999. A.A. Balkema, Rotterdam. pp. 681–686.

McConnell, R.G., and Brock, R.W. 1904. Report on the great landslide at Frank, Alberta. Annual Report for 1903. Department of the Interior, Ottawa, Ontario. Part 8. pp. 17.

Oda, M., and Konishi, J. 1974*a*. Microscopic deformation mechanism of granular material in simple shear. Soils and Foundations, **14**(4): 25–38.

Oda, M., and Konishi, J. 1974*b*. Rotation of principal stresses in granular material during simple shear. Soils and Foundations, **14**(4): 39–53.

Oger, L., Savage, S.B., Corriveau, D., and Sayed, M. 1998. Yield and deformation of an assembly of disks subjected to a deviatoric stress loading. Mechanics of Materials, **27**: 189–210.

Ohashi, T., and Matsuoka, H. 1995. Microscopic study on cohesion of wet aluminum rods mass. *In* Proceedings of the 50th Annual Conference of the Japan Society of Civil Engineers (JSCE), Ehime, Japan, 19–21 September 1995. Japan Society of Civil Engineers (JSCE). Vol. III-164, pp. 328–329.

Prior, I.G. 1992. The geotechnical advantages and disadvantages of pneumatic soil nailing. *In* The Engineering Group of the Geological Society of London, 28th Regional Conference. Preprints. The Engineering Group of the Geological Society of London, Manchester.

Raju, G.V.R., Wong, I.H., and Low, B.K. 1997. Experimental nailed soil walls. Geotechnical Testing Journal, ASTM, **20**(1): 99–102.

Rothenburg, L., and Bathurst, R.J. 1989. Analytical study of induced anisotropy in idealized granular materials. Géotechnique, **39**(4): 601–614.

Schlosser, F., Plumelle, C., Unterreiner, P., and Benoit, J. 1992. Failure of full-scale experimental soil nailed wall by reducing the nails length. *In* Proceedings of the 2nd International Conference on Earth Reinforcement Practice, IS Kyushu '92, Kyushu, Japan. A.A. Balkema, Rotterdam. pp. 531–535.

Shewbridge, S.E., and Sitar, N. 1990. Deformation-based model for reinforced sand. Journal of Geotechnical Engineering, ASCE, **116**(7): 1153–1170.

Skinner, A.E. 1969. note on the influence of interparticle friction on the shearing strength of a random assembly of spherical particles. Géotechnique, **19**(1): 150–157.

Xanthako, P.P. 1991. Ground anchors and anchored structures. John Wiley & Sons, Inc., New York.

Yamamoto, S. 1995. Fundamental study on mechanical behavior of granular materials by DEM. Ph.D. thesis, Nagoya Institute of Technology, Nagoya, Japan. [In Japanese.]